scientific reports

Check for updates

OPEN

Efficient defluoridation of high-fluoride water using rare earth-based adsorbents: adsorption performance, mechanism, and kinetics

Hongwei Du[1,3], Lingxian Fang[2], Xinghao Shi[2], Tongtong Li[2], Zifeng Sui[2], Jinshan Zhong[2] & Ke Li[2]✉

This study investigated the adsorption behaviour of fluoride ions from fluorine-containing solutions at a defined concentration using Ce^{3+} and hydrogen peroxide. The influences of adsorption time, solution pH, adsorbent dosage, initial fluoride ion concentration, and coexisting ions on adsorption efficiency were systematically assessed. The results demonstrated that the adsorbent exhibited high adsorption performance at ambient temperature, achieving a saturated adsorption capacity between 114.47 and 118.43 mg/g. The synergistic action of Ce^{3+} and H_2O_2 provided dual adsorption–precipitation pathways, in which thermodynamically stable CeF_3 formed through ion exchange while surface Ce^{4+}–OH sites produced by oxidation further captured fluoride via ligand exchange. The adsorption kinetics conform to the pseudo-second-order model, and the equilibrium data fit both the Langmuir and Freundlich isotherm models. Sulphate ions promoted fluoride removal, whereas chloride and nitrate ions had little effect; however, bicarbonate and carbonate ions strongly inhibited this process. These findings demonstrate that the Ce^{3+}/H_2O_2 system offers a robust, cost-effective, and regenerable approach with good tolerance to coexisting anions. Overall, this work not only elucidates the dual mechanism of Ce-based defluoridation but also provides a practical strategy for developing rare-earth-based adsorbents for sustainable and high-efficiency water purification.

Keywords Fluoride removal, Ce^{3+}/H_2O_2 system, Adsorption mechanism, Rare earth–based material, Wastewater treatment

Fluoride pollution poses a persistent threat to global drinking water safety and ecosystems. While trace amounts of fluoride are essential for human health, long-term excessive intake can cause serious diseases such as dental and skeletal fluorosis[1]. To protect public health, the World Health Organization(WHO) has set the maximum permissible fluoride concentration in drinking water at 1.5 mg/L[2]. Exceeding this threshold has been directly linked to the onset of dental and skeletal fluorosis, which poses long-term health risks[3]. For industrial wastewater, China has stipulated discharge limits for fluoride in the national Integrated Wastewater Discharge Standard (GB 8978-1996), requiring concentrations not to exceed 10–20 mg/L depending on the discharge category[4]. Industries such as metallurgy, electronic manufacturing, electroplating, and semiconductors are major sources of fluoride-containing wastewater, and their discharge is one of the important reasons for groundwater contamination[5]. It is estimated that about 200 million people worldwide are exposed to fluoride-contaminated water, and in China the number of people affected by endemic fluorosis is very large[6,7]. This issue has already become a serious obstacle to the sustainable use of water resources[8]. These finding indicate that fluoride control is not only an environmental problem, but also a challenge to public health and industrial regulation.

At present, the common techniques for fluoride removal include chemical precipitation, ion exchange, membrane technologies, electrodialysis, the Nalgonda method, and adsorption[9]. Chemical precipitation

[1]School of Mining and Coal, Inner Mongolia University of Science and Technology, Baotou 014010, China. [2]School of Energy and Environment, Inner Mongolia University of Science and Technology, Baotou 014010, China. [3]Inner Mongolia Key Laboratory of Mining Engineering, Baotou 014010, China. ✉email: lklk@imust.edu.cn

is suitable for high-concentration fluoride wastewater, but it requires large doses of reagents and may cause secondary pollution[10]. Ion exchange is effective but relies on expensive resins, and the regeneration process produces waste liquid that limits its large-scale use. Membrane technology can remove fluoride efficiently, but it has a high cost, complicated operation, and also removes beneficial minerals[6]. Electrodialysis is not widely used because of high energy consumption, electrode passivation, and scaling problems[11,12].The Nalgonda method is simple and low-cost, but the treated water often shows large pH changes[13]. In general, each technology has its own advantages and disadvantages, but the problems of cost, energy, and secondary pollution limit its wide application. Compared with these methods, adsorption has remarkable advantages because of its simple operation, high efficiency, and relatively low cost.

Among the many adsorbents, rare-earth-based materials have attracted great attention because of their special high affinity for fluoride ions through Lewis acid–base interactions[14]. Significant progress has been made in exploring the use of rare earths such as Ce^{3+} and La^{3+} for fluoride removal. Japanese researchers reported the effective coordination of multivalent rare-earth ions with fluoride[15], whereas Raichur et al. demonstrated that rare-earth oxides efficiently remove fluoride without significant interference from common ions[16]. Gonzales et al. Reported that cerium chloride could remove nearly 90% of fluoride from wastewater, even under high-fluoride conditions, with sulphate and phosphate ions enhancing the adsorption, whereas nitrate had little effect[17]. Zuniga-Muro et al. further reported that Ce^{4+}-modified bone charcoal exhibited superior chemical stability and antibacterial properties compared to Ce^{3+}-modified bone charcoal, although its adsorption capacity was relatively modest[18]. Previous studies have also demonstrated the effectiveness of Mg–Ce–La composites[19], La/Ce-modified alumin[20], and mixed rare-earth oxides[16] for fluoride removal. These findings confirm the great potential of rare-earth-based adsorbents for fluoride remediation.

In recent years, researchers have developed more practical rare-earth sorbents. For example, composites of rare earth elements with carbon nanomaterials[21] or biopolymers[22] have been designed to increase the dispersion and stability of active sites. In addition, controlling the morphology and defect structure of cerium oxides can significantly improve adsorption capacity and kinetics[23]. Progress in characterization techniques such as X-ray photoelectron spectroscopy (XPS) and electron microscopy has further provided molecular-level insights into adsorption mechanisms and structure–property relationships[21,23]. Despite these advances, the widespread application of rare-earth sorbents faces four critical challenges: (1) the complex and costly synthesis of many high-performance materials; (2) an insufficient understanding of their long-term stability and regenerability; (3) a lack of validation in real wastewater matrices with competing anions and organic matter; and (4) an underexplored environmental footprint across their full life cycle. These issues represent major bottlenecks hindering the translation of laboratory findings into practical engineering applications.

To address these challenges, this study proposes a novel adsorption system based on the synergistic effect of Ce^{3+} and hydrogen peroxide (H_2O_2). The novelty of this system is threefold: First, in terms of cost, it utilizes inexpensive, commercially available precursors under ambient conditions, avoiding energy-intensive synthesis. Second, in performance, it achieves a high adsorption capacity surpassing that of conventional Ce^{3+}-only systems. Third, with respect to reliability, it maintains high efficiency across a broad pH range and exhibits strong resilience against common coexisting anions. The adsorption behavior was systematically investigated. To verify these merits, the adsorption behavior was systematically examined with respect to the solution pH, adsorbent dosage, initial fluoride concentration, and the presence of competing anions, and the underlying mechanism was further clarified using advanced characterization techniques (SEM, EDS, FTIR, and XPS). Overall, this study aims to clarify the adsorption mechanism and provide new insights into the development of efficient and sustainable defluoridation technologies.

Materials and methods

Materials

The rare earth nitrate used in this study (99.99% purity; Sinopharm Chemical Reagent Co., Ltd., China) had a cerium content in the rare earth nitrate was 322.7 g/kg. This material was received in the form of crystal particles and used as an adsorbent. The chemical reagents utilised in this study included sodium fluoride, sodium chloride, sodium carbonate, sodium bicarbonate, sodium sulphate, sodium nitrate, sodium hydroxide, and hydrochloric acid, all of which were of analytical grade. pH adjustments were performed using diluted 1 mol/L HCl or 1 mol/L NaOH solutions. Deionised water was used throughout the experimental procedures. A synthetic high-fluoride water sample was prepared by dissolving sodium fluoride in deionised water to simulate fluoride-contaminated water conditions.

Adsorption experiment

A total of 2.2 g of anhydrous sodium fluoride was dissolved in deionised water and then diluted to 1000 mL in a volumetric flask to prepare a fluoride stock solution. The stock solution was stored in a polytetrafluoroethylene bottle for future use. The stock solution was diluted as needed to prepare fluoride solutions of different concentrations. All fluoride removal experiments were conducted in 250 mL polypropylene conical flasks. pH adjustment was performed using 0.1 mol/L hydrochloric acid and 0.1 mol/L sodium hydroxide solutions. Except for the experiments investigating the effects of initial fluoride concentration and isothermal adsorption, all the other experiments were conducted with an initial fluoride concentration of 100 mg/L and a constant shaking speed of 150 rpm. For fluoride ion concentration measurements using a fluoride ion-selective electrode, a total ionic strength adjustment buffer (TISAB) was added at a 1:1 volume ratio. Each experiment was conducted in triplicate to ensure reproducibility. While maintaining all other parameters were held constant, the following variables were systematically altered: initial pH (5–8), adsorbent dosage (0.5–2.5 g/L), contact time (0–120 min), initial fluoride concentration (5–150 mg/L), presence of competitive ions (Cl^-, NO_3^-, SO_4^{2-}, CO_3^{2-}), and adsorption temperature (20 °C, 30 °C, and 40 °C). A specified amount of cerium nitrate hexahydrate and

30% hydrogen peroxide solution (to oxidise cerium ions in the solution) was added, followed by shaking in a thermostatic water bath shaker for a designated duration. The solution was then filtered, and the filtrate was used to determine the fluoride ion concentration. After each adsorption cycle, the spent adsorbent was regenerated with 0.1 mol L^{-1} NaOH solution for 30 min under stirring, followed by washing and reuse under identical conditions. The adsorption capacity (q_e) and removal efficiency (η) were calculated according to Eqs. (1) and (2), following the methods described in Refs[24] and Refs[6], respectively.

$$q_e = \frac{(C_0 - C) \times V}{W} \tag{1}$$

$$\eta\,(\%) = \frac{(C_0 - C)}{C_0} \times 100 \tag{2}$$

where q_e represents the adsorption capacity (mg/g), and C_0 and C represent the concentration of F^- before adsorption and the fluoride ion concentration at equilibrium (mg/L), respectively. V represents the volume of the reaction mixture (L), and W represents the dry weight of the adsorbent (g).

Characterisation and analysis methods

The fluoride ion concentrations were determined using a fluoride ion-selective electrode (PXSJ-216F, Shanghai). The surface structure of the adsorbent was characterised by scanning electron microscopy (SEM; Thermo Scientific Axia ChemiSEM, USA), and elemental composition analysis was conducted using energy-dispersive X-ray spectroscopy (EDS). The functional groups were identified through Fourier transform infrared (FTIR) spectroscopy (Thermo Nicolet IS5, USA) within the spectral range of 400–4000 cm^{-1}. For FTIR measurements, the adsorbent was ground with an agate mortar, blended with KBr, and compressed into pellets using a mechanical press. The crystalline phases of the samples before and after fluoride adsorption were analysed via X-ray diffraction (XRD; Bruker D8 Advance, Cu Kα radiation, 40 kV, 40 mA, 2θ = 10°–80°). Surface zeta potential was measured using a Zetasizer Nano ZS90 (Malvern Instruments, UK) to determine the point of zero charge (pH_pzc) and evaluate the effect of surface charge on adsorption. The Ce content of the adsorbent before and after fluoride adsorption was quantified by inductively coupled plasma optical emission spectrometry (ICP–OES; PerkinElmer Optima 8300, USA) after acid digestion, to assess the participation of Ce species during the defluoridation process. To elucidate the fluoride removal mechanism, X-ray photoelectron spectroscopy (XPS; Thermo Fisher Escalab 250Xi, USA) was employed.

Statistical Analysis

All adsorption experiments were carried out in triplicate, and the mean values were reported. The standard deviations (error bars) in the figures represent the variability among the three independent measurements. The same batch of adsorbent was used for repeated tests to ensure reproducibility.

Adsorption kinetic and isotherm parameters, as well as correlation coefficients (R^2), were obtained using Origin 2021 software through nonlinear least-squares fitting of the corresponding model equations.

Results and discussion

Characterisation studies

SEM and EDS analyses

SEM was used to observe the surface morphology of the adsorbent before and after fluoride adsorption, and the corresponding images are presented in Fig. 1. As shown in Fig. 1a and c, the unloaded adsorbent has a rough and heterogeneous surface with visible pores and irregular aggregates, providing many potential active sites for fluoride uptake. After fluoride adsorption (Fig. 1b and d), the surface become denser and smoother, indicating that fluoride species have been successfully deposited on the adsorbent surface.

The surface composition of the adsorbent before and after fluoride adsorption was further examined by EDS, as shown in Fig. 1e–f. Before adsorption, the surface mainly contained oxygen (76.5 at.%) and cerium (23.5 at.%), suggesting the presence of Ce–O compounds. After adsorption, a clear fluorine peak appeared, and the atomic percentage of fluorine reached 58.7 at.%, whereas that of oxygen decreased to 18.3 at.% and that of cerium remained almost unchanged (23.0 at.%). These changes indicate that fluoride ions were successfully attached to the surface and replaced part some of the oxygen species.

The calculated Ce/O and Ce/F ratios (0.307 and 0.391, respectively) further support the formation of Ce–F bonds on the surface. This result agrees well with the SEM observations, which showed that the surface became smoother and denser after adsorption. Together, the SEM and EDS results confirmed that fluoride was effectively captured on the adsorbent through chemical interactions rather than simple physical attachments.

FTIR studies

To evaluate the functional groups of the adsorbent before and after fluoride removal, FTIR spectral analysis was conducted (Fig. 2).The Ce–O bond exhibits a stretching vibration peak at 844 cm^{-1}, which decreases in intensity following fluoride ion adsorption, suggesting the involvement of cerium in the adsorption process[25]. A prominent OH stretching vibration peak is detected at 3418 cm^{-1}[26], and its increased intensity after adsorption reflects the migration of hydroxyl groups, confirming their role in fluoride binding. The peak corresponding to Ce-OH at 1051 cm^{-1} also shows a reduced intensity, whereas the metal–oxygen band within the 400–600 cm^{-1} range weakens, indicating electrostatic interactions between Ce^{4+} ions and fluoride ions[27,28]. Furthermore, after fluoride adsorption, the peaks at 844 cm^{-1} and 1051 cm^{-1} shifted to 854 cm^{-1} and 1062 cm^{-1}, respectively, indicating structural modifications in the oxide framework upon fluoride incorporation[29].

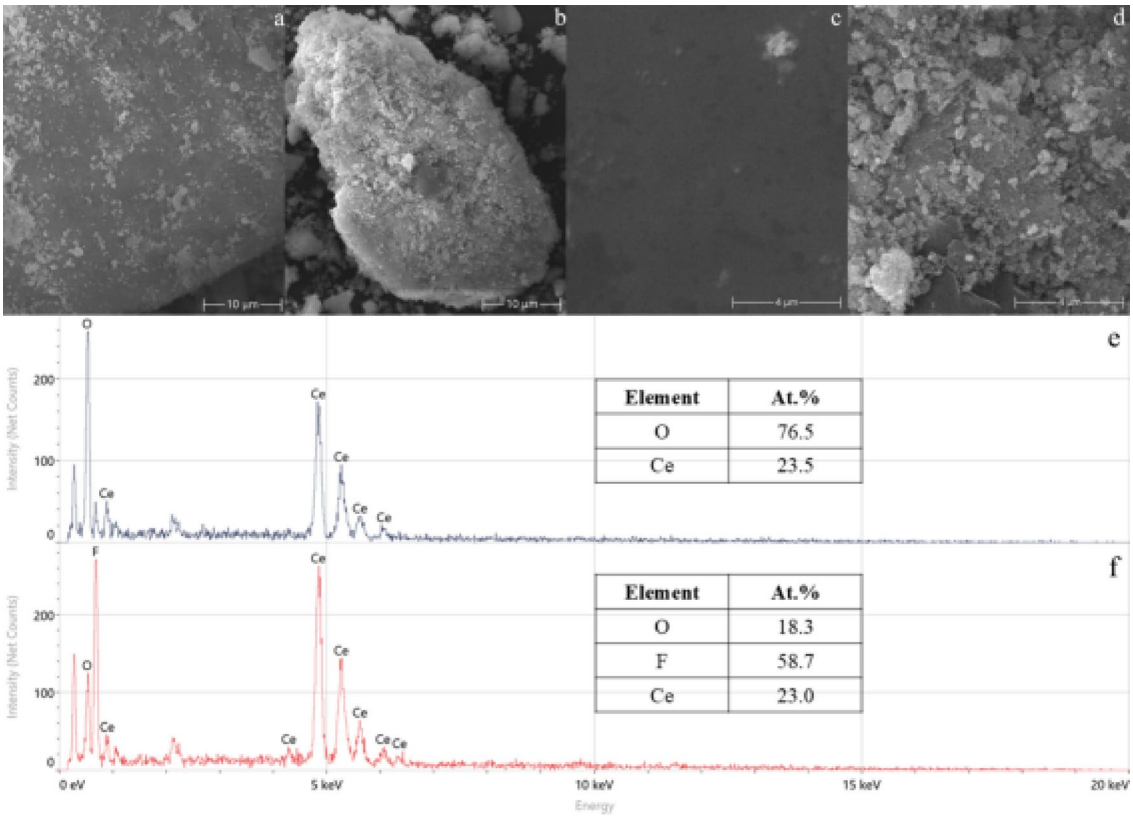

Fig. 1. (**a**) SEM image of (**a**) unadsorbed fluorine at 10 μm (**b**) fluoride adsorption at 10 μm(**c**) unadsorbed fluorine at 4 μm (**d**) fluoride adsorption at 4 μm(**e**) EDS energy spectrum of unadsorbed fluoride(**f**) EDS energy spectrum after fluoride adsorption.

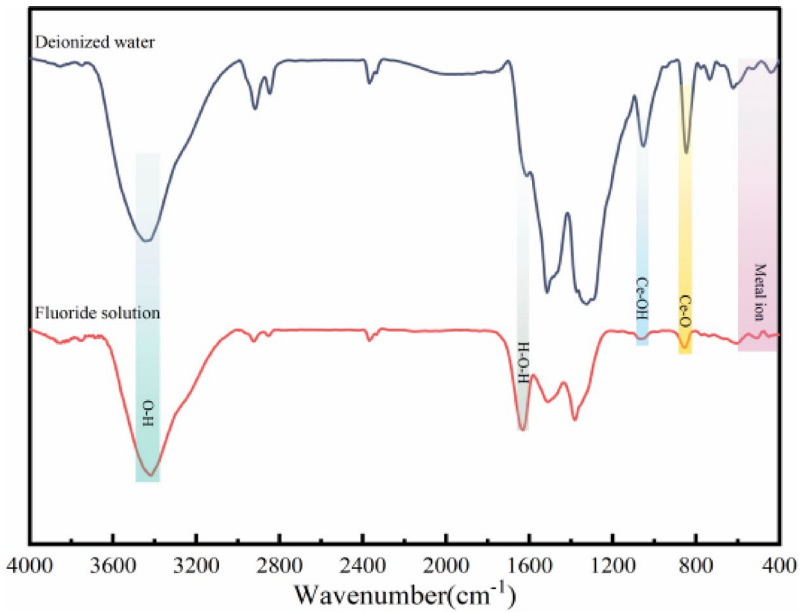

Fig. 2. FTIR results for unadsorbed fluoride and after fluorine adsorption.

XRD studies

The XRD pattern of the solid product after fluoride adsorption (Fig. 3) shows two crystalline phases: CeF_3 (PDF#97-005-6773) and cubic fluorite-type CeO_2 (PDF#97–016-9031).

The appearance of CeF_3 peaks indicates that fluoride ions reacted with Ce^{3+} species to form a stable fluoride compound, confirming that chemical precipitation was one of the main mechanisms of fluoride removal. Moreover, the presence of residual CeO_2 suggested that a portion of Ce remained in the oxidized state, and its surface hydroxyl groups (Ce–OH) participated in ligand exchange with fluoride ions. Quantitative analysis using ICP–OES further supported these findings. A slight decrease in the Ce content of the solid phase was detected after adsorption, which corresponds well with the formation of CeF_3 identified by XRD.

Therefore, the overall defluoridation process involves a combination of Ce^{3+}–F^- precipitation and Ce^{4+}–OH surface complexation, which together ensure both high removal efficiency and strong binding stability of fluoride on the adsorbent surface.

XPS studies

To further investigate the mechanism of fluoride ion removal, XPS characterisation was performed on samples before and after fluoride ion adsorption (Fig. 4). The overall spectrum shows that fluoride ions are effectively adsorbed. By observing the peak shapes in the XPS Ce 3d spectra before and after fluoride ion adsorption, different oxidation states can be distinguished and attributed (Fig. 4a). The peaks at 880, 885, 898, and 903 eV correspond to the Ce^{3+} state, whereas the peaks at 882, 888, 899, 901, 908, and 917 eV correspond to the Ce^{4+} state[30,31]. XPS data confirmed that the adsorbent used in this study contained both Ce^{3+} and Ce^{4+} before and after fluoride ion adsorption. Owing to the high electronegativity of F^-, its binding with Ce reduces the electron density and increases the binding energy. Therefore, the Ce 3d peaks shift toward higher binding energies after adsorption. Analysis of the O 1 s spectrum revealed four distinct peaks corresponding to C–O, C = O, Ce^{3+}–O, and Ce^{4+}–O species (Fig. 4b). The dominant peak at a binding energy of 529 eV is attributed to Ce^{4+}–O, whereas the peak at 530 eV corresponds to Ce^{3+}–O[32,33]. Given the close similarity in ionic radii between F^- (0.133 nm) and OH^- (0.140 nm) ions[34], it is likely that fluoride ions substituted for hydroxide ions on the adsorbent surface through ion exchange. Post-adsorption, the emergence of an F 1 s peak at 684.5 eV (Fig. 4c) confirms the chemical binding of fluoride ions, indicating successful adsorption. The strong electronegativity of fluoride results in a reduction in electron density upon bonding with cerium, leading to a shift of the Ce 3d peak toward higher binding energy values.

Effect of solution pH

The pH of the reaction medium is one of the main factors affecting the adsorption capacity. Therefore, the influence of the initial pH on the adsorption of F^- by the adsorbent was investigated. The dosage of the fluoride mixture was 0.2 g, the volume of the reaction mixture was 200 mL, the reaction time was 30 min, and the initial concentration of F^- was 100.0 mg/L. The influence of pH on the adsorption capacity was studied within the pH range of 5.0–8.0, and the results are shown in the Fig. 5a. The adsorption capacity and removal rate both decrease gradually with increasing pH. The fluoride removal efficiency remained above 90% between pH 5.0 and 6.0, indicating favorable conditions for adsorption within this range. This can be attributed to strong electrostatic attraction between the positively charged surface (Ce–OH_2^+) and fluoride ions, as well as to complexation and precipitation of CeF_3. When the pH increases above 6.5, the adsorption capacity decreases due to increasing competition from hydroxyl ions and the gradual reduction in the positive surface. Nevertheless, the adsorbent still maintains good performance at pH values between 7.0 and 8.0, highlighting its broad adaptability and stability under near-neutral conditions.

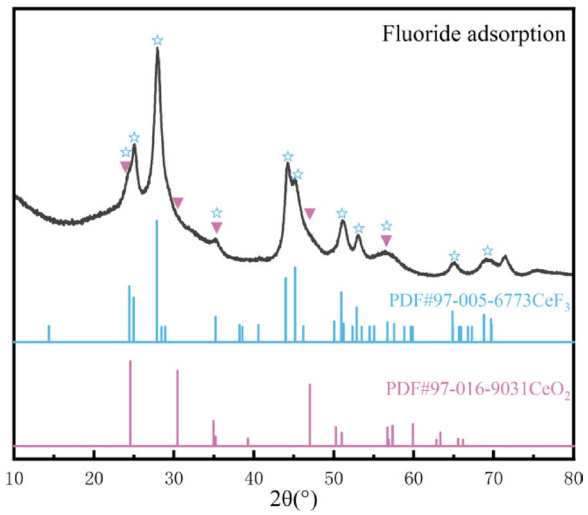

Fig. 3. XRD pattern after fluorine adsorption.

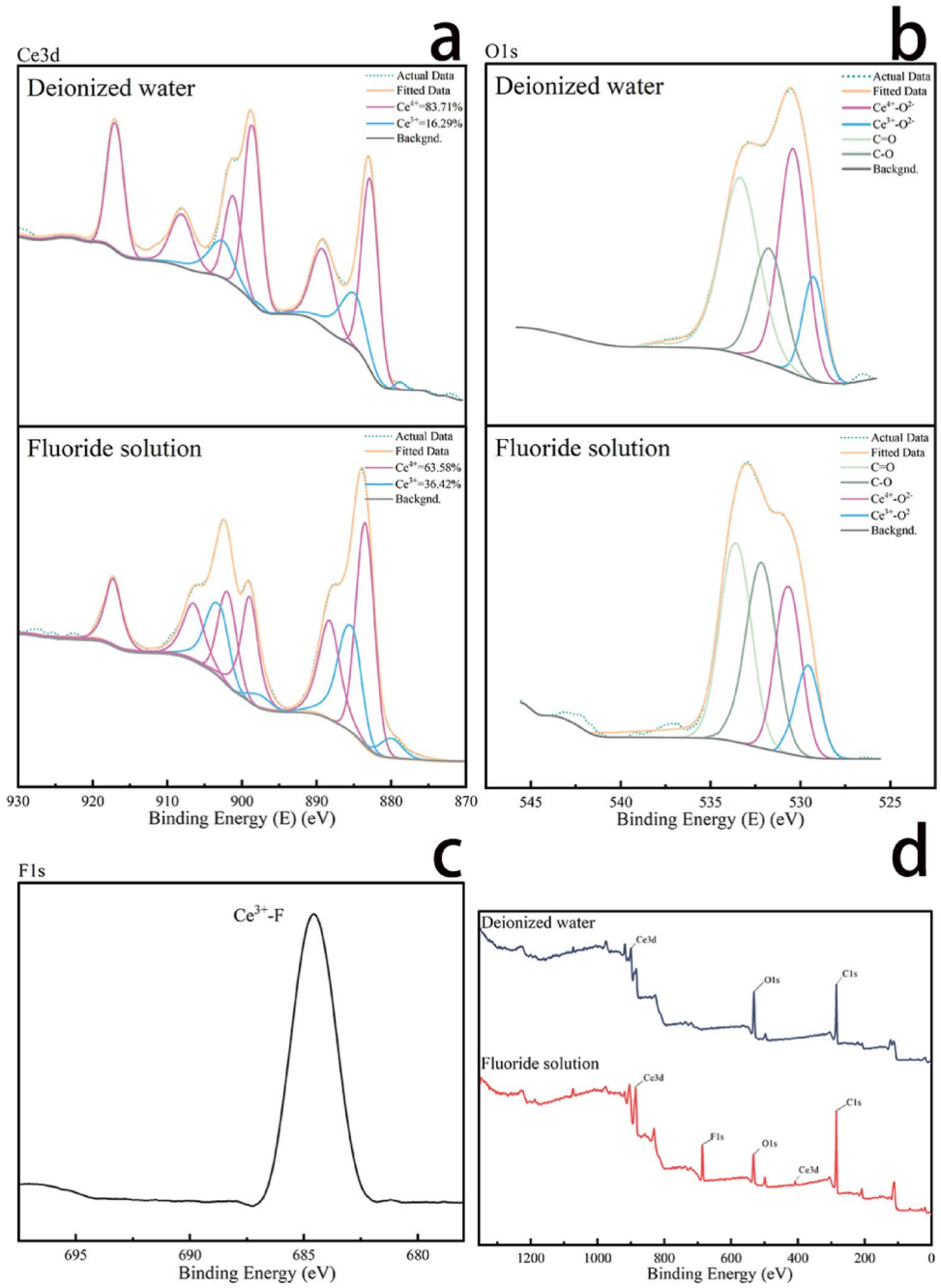

Fig. 4. XPS spectra of the adsorbent before and after fluoride adsorption: (**a**) Ce 3d, (**B**) O 1 s, (**c**) F 1 s, (**d**) Total survey spectrum. The spectra labelled "Deionized water" and "Fluoride solution" represent the samples before and after fluoride adsorption, respectively. The purple line in Ce 3d corresponds to the oxidation state of Ce^{4+}, and the blue line represents Ce^{3+}

Zeta potential analysis demonstrated that pH influences the adsorption capacity by regulating the surface charge of the adsorbent (Fig. 5b). As the pH increases, the surface charge shifts from positive to negative, crossing the isoelectric point (IEP) at pH 6.9. The high stable adsorption capacity observed within the pH range of 5.0 to 6.0 corresponds precisely to a state of strongly positive zeta potential. This state promotes favorable electrostatic attraction between the adsorbent and fluoride ions (F^-), thereby enhancing adsorption mechanisms such as complexation and CeF_3 precipitation. Conversely, the progressive decline in adsorption capacity between pH values of 6.9 and 8.0 correlates directly with the zeta potential shifting to negative values. Within this range, F^- ions induce electrostatic repulsion, while the competitive effect of OH^- ions intensify[35]. Crucially, the maintenance of significant adsorption capacity even when the zeta potential becomes negative indicates that the adsorption process is not solely governed by electrostatic interactions. Throughout the entire pH range, the

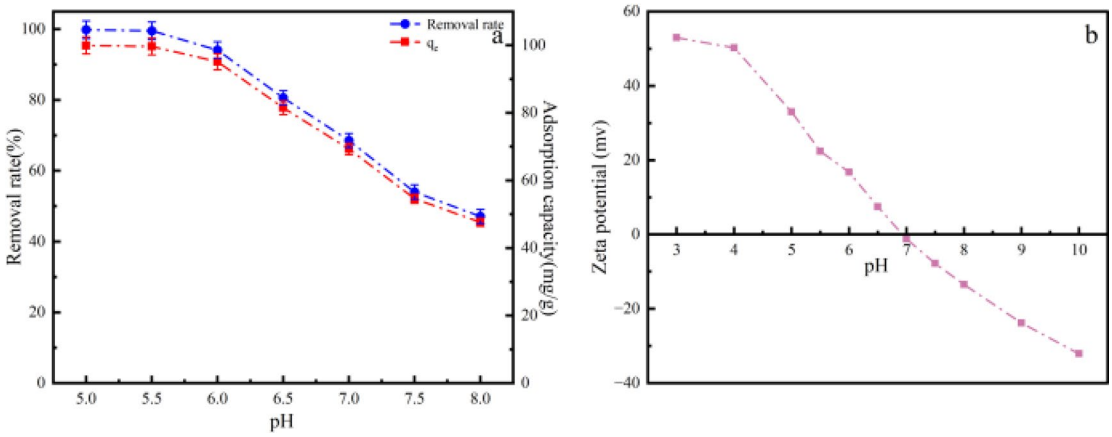

Fig. 5. (**a**)Effect of solution pH(**b**) zeta potential of adsorbent (adsorbent dose 1 g/L, contact time 30 min, initial concentration 100 mg/L).

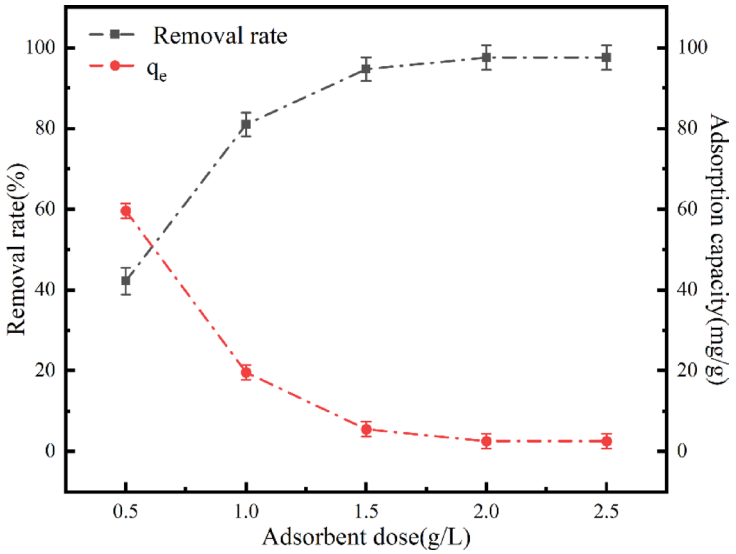

Fig. 6. Effect of solution adsorbent dosage.

synergistic effects of electrostatic attraction, complexation, and precipitation demonstrate the broad adaptability and formidable practical application potential of this material.

Effect of dosage

The influence of adsorbent dosage on the fluoride removal rate is shown in the Fig. 6. The fluoride removal rate of the 0.5–2.5 g/L adsorbent increased from 42.22% to 97.55%. However, when the dosage of the adsorbent exceeded 2.0 g/L, there was no significant change in the removal rate of fluoride. Considering the removal efficiency and financial cost, in all subsequent experiments, an adsorbent dosage of 2.0 g/L was used as the optimal dosage.

Effect of initial fluoride concentration

The adsorption of fluoride by rare earth elements was studied. The initial fluorine concentration was 5–150 mg/L, the optimal adsorbent dosage was 1.0 g/L, the temperature was 303 K, and the contact time was 30 min. The results are shown in Fig. 7. The fluoride removal rate gradually increasing with initial fluoride concentration. The fluorine adsorption capacity increases with increasing initial fluorine concentration. Gonzales J M et al. reported a similar trend[17].

Effect of interfering ions

Typically high-fluoride water contains not only fluoride ions but also other anions such as chloride (Cl^-), nitrate (NO_3^-), bicarbonate (HCO_3^-), sulphate (SO_4^{2-}), and carbonate (CO_3^{2-}). To evaluate the potential interference from coexisting anions, solutions containing fluoride (initial fluoride ion concentration = 100 mg/L, adsorbent

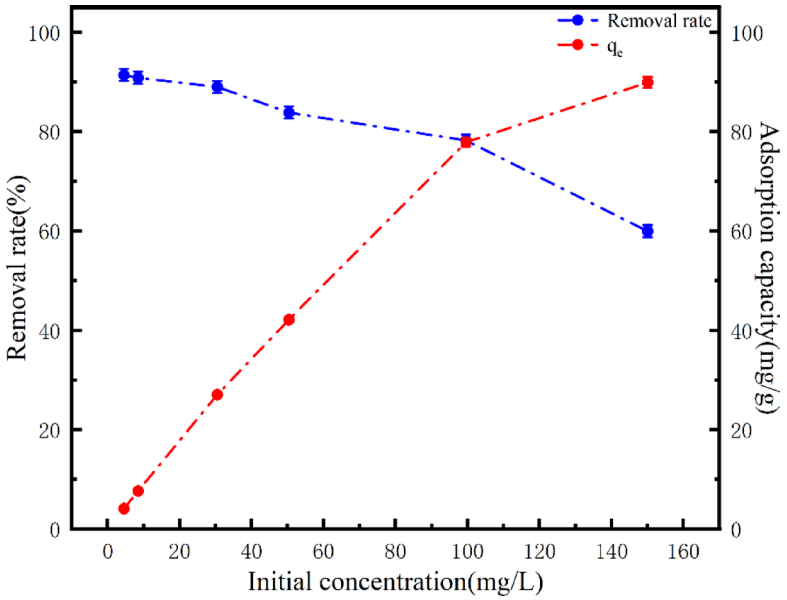

Fig. 7. Effect of initial fluoride concentration.

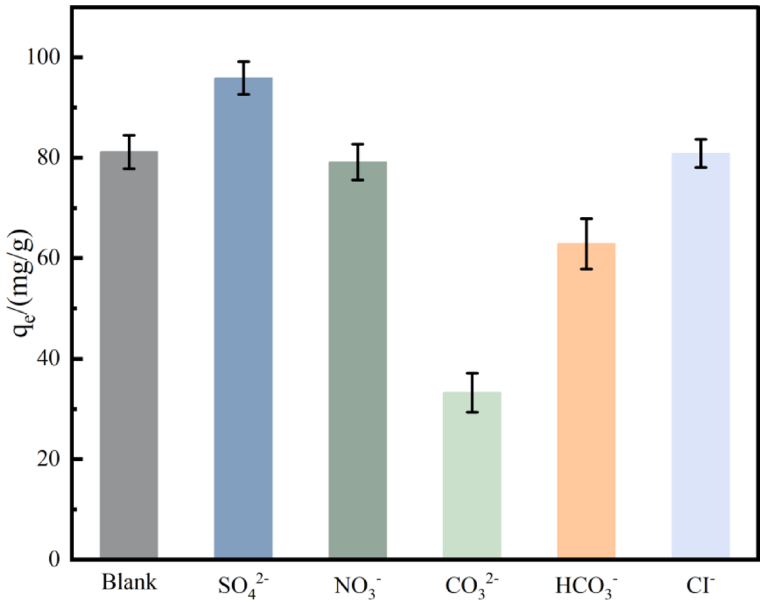

Fig. 8. Effect of coexisting anions on the fluoride adsorption capacity (q_e). Adsorbent dose = 1 g L^{-1}, contact time = 30 min, initial fluoride concentration = 100 mg L^{-1}, and coexisting anion concentration = 200 mg L^{-1}.

dosage = 1 g/L) were supplemented with Cl^-, NO_3^-, CO_3^{2-}, and SO_4^{2-} at a concentration of 200 mg/L to assess the adsorbent's interference resistance. The corresponding results are presented in Fig. 8.The blank removal was 81.16%. In the presence of SO_4^{2-}, removal increased to 95.86% (promotion). Cl^- and NO_3^- caused only minor changes (80.85% and 79.15%, respectively). In contrast, HCO_3^- and CO_3^{2-} markedly suppressed removal (57.18% and 33.24%, respectively).

Overall influence: SO_4^{2-} (promotion) $\gg Cl^- \approx NO_3^-$ (minor) $> HCO_3^- > CO_3^{2-}$ (strong inhibition).

This pattern is consistent with the ion properties and surface chemistry of Ce-based sorbents: SO_4^{2-} can compress the electrical double layer/bridge particles and thus facilitates F^- uptake; Cl^- and NO_3^- are weakly coordinating monovalent anions and show little competition; carbonate species hydrolyze ($CO_3^{2-} + H_2O \rightleftharpoons HCO_3^- + OH^-$), raise the OH^- level and compete with F^- (and can form surface carbonate species), consequently depressing fluoride adsorption[36].

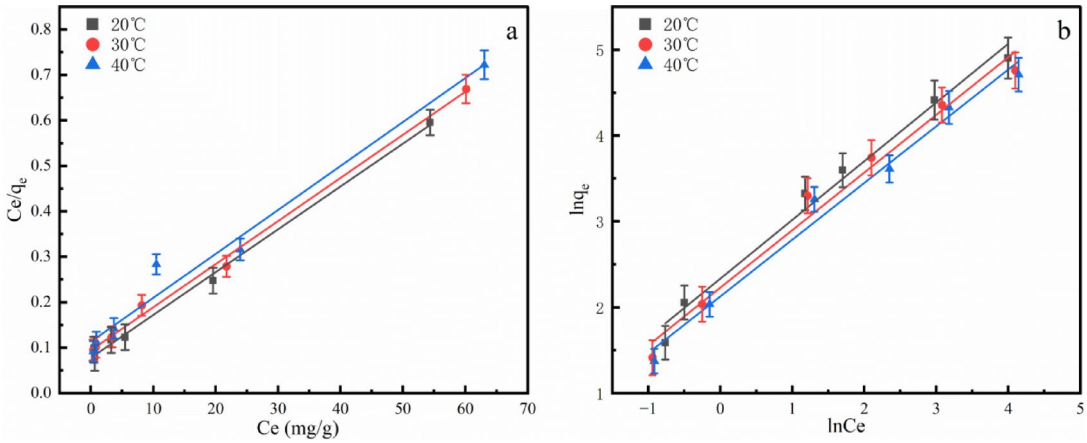

Fig. 9. Adsorption isotherm model (**a**) Langmuir (**b**) Freundlich.

	Langmuir				Freundlich		
T(°C)	Q_{max}(mg/g)	K_L	R^2	R_L	K_F	n	R^2
20	118.43	0.107	0.998	0.058651	18.943	1.986452	0.946
30	114.47	0.093	0.991	0.06689	16.901	2.01001	0.94
40	110.535	0.067	0.974	0.090498	14.264	2.199881	0.941

Table 1. Adsorption isotherm parameters.

Adsorbent	pH	Q_m(mg/g)	References
Magnetic bone biochar[37]	8.0	5.23	(Zhou et al., 2019)
Fe-La composite[38]	3.8–7.1	27.42	(Wang et al., 2018a)
MCH-La[39]	7.0	136.78	(Dong et al., 2016)
Al-Zr-La tri-metal hydroxide[40]	3.0	90.48	(Zhou et al., 2018)
Zirconium-impregnated Camellia seed biochar[41]	3.0–11.0	11.04	(Mei et al., 2020)
Mg-Al-La tri-metal oxide[42]	4.0–10.0	31.72	(Wang et al., 2017a)
PPBC-La[43]	6.5	19.86	(Wang et al., 2017b)
Calcined kaolin/hydroxyapatite[21]	3.0	126.56	(El Messaoudi et al., 2024)
This study	5.0–7.0	118.43	This study

Table 2. Comparison of the fluoride adsorption capacities of various adsorbents reported in the literature.

Adsorption isotherm studies

To analyse the equilibrium behaviour in the adsorption process, the Langmuir and Freundlich isotherm models were used to fit the experimental data of the adsorption of F-by the adsorbent. The fitting results are shown in Fig. 9 and Table 1. The experimental data for F^- adsorption yielded correlation coefficients (R^2) greater than 0.939 for both models, demonstrating that each provides a satisfactory representation of the adsorption process. This suggests that the fluoride adsorption behaviour aligns well with the assumptions of both isotherm models. Furthermore, an R_L of 0.597 ranging from 0 to 1 indicates that this adsorption behaviour is spontaneous and is a type of preferential adsorption. $n > 1$, $R^2 > 0.94$, and the fitting correlation is good, indicating that this adsorption process is an adsorption mode that combines monolayer coverage and multilayer adsorption. When the temperature is increased, the saturated adsorption capacity decreases, indicating that increasing the temperature is not conducive to the adsorption reaction. The observed inverse relationship unequivocally indicates that fluoride adsorption constitutes an exothermic process, wherein desorption under elevated temperatures has a greater thermodynamic advantage relative to adsorption. The calculated standard enthalpy change ΔH° yields a negative value further corroborating the exothermic nature of this process.

Comparison of adsorption performance with reported adsorbents

To further evaluate the competitiveness of the Ce^{3+}/H_2O_2 adsorbent, its fluoride removal capacity was compared with that of other adsorbents reported in the literature (Table 2).

A comparison of the maximum adsorption capacities (Q_m) of different fluoride adsorbents reported in the literature is shown in Table 2. The Ce^{3+}/H_2O_2 adsorbent developed in this study had a Q_m of 118.43 mg g^{-1},

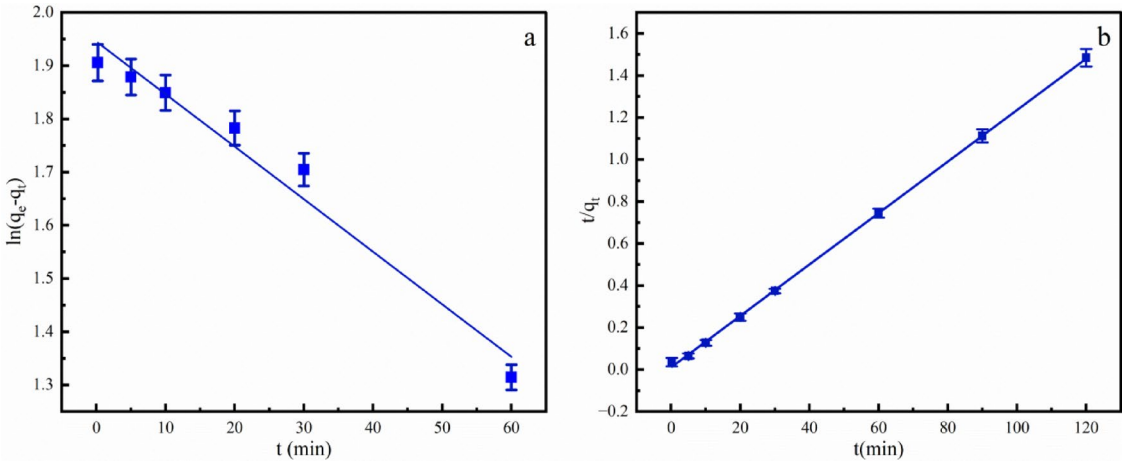

Fig. 10. Adsorption kinetics: (**a**) Pseudo-first-order and (**b**) Pseudo-second-order models.

	K(g/mg·min)	q_e(mg/g)	R^2
Pseudo-first-order	0.02273	80.623	0.9614
Pseudo-second-order	0.01377	81.699	0.9996

Table 3. Adsorption kinetics parameters.

which is close to that of high-performance materials such as MCH–La (136.78 mg g^{-1}) and calcined kaolin/hydroxyapatite (126.56 mg g^{-1}). However, most of these adsorbents work well only under strongly acidic conditions (around pH 3.0), whereas the Ce^{3+}/H_2O_2 adsorbent maintains high removal efficiency over a wider and more practical pH range of 5.0–8.0.

Compared with many biomass-based or tri-metallic materials, the Ce^{3+}/H_2O_2 system also shows better stability and reusability, which makes it more suitable for real wastewater treatment. This combination of high capacity, broad pH adaptability, and good recyclability suggests that the Ce^{3+}/H_2O_2 adsorbent has strong potential for real-world fluoride removal.

Kinetics studies

The Fig. 10 shows that during the initial stage of F^- adsorption, the data exhibit good linearity, suggesting that the pseudo-first-order kinetic model is applicable at the early phase of the process. However, as adsorption progresses, deviations from linearity become evident, indicating that this model does not accurately describe the entire adsorption behaviour. The corresponding Table 3 confirms this observation, as the pseudo-first-order model yields a relatively low correlation coefficient (R^2) and a calculated *qe* value that deviates from the experimentally measured value. In contrast, the pseudo-second-order kinetic plot for F^- adsorption demonstrated a strong fit across the entire time range. The kinetic parameters summarised in the Table 3 show that the correlation coefficients ($R^2 > 0.99$) and close agreement between the calculated and experimental adsorption capacities indicate that the pseudo-second-order model best describes the process, suggesting that chemical adsorption involving valence forces or electron exchange dominates the fluoride uptake. Combined with the Langmuir isotherm fit, which reflects monolayer adsorption on a homogeneous surface, these results point to a mechanism governed by Ce–F complexation and CeF_3 precipitation, which is consistent with the findings from the XRD and XPS analyses. Therefore, the kinetic evidence provides quantitative support for the proposed dual defluoridation mechanism illustrated, in which both precipitation and surface complexation contribute synergistically to fluoride removal.

Thermodynamic treatment of the fluoride sorption process

The thermodynamic parameters associated with the adsorption, standard free energy change(ΔG°), standard enthalpy change(ΔH°) and standard entropy change (ΔS°) were calculated as follows.

The free energy of the sorption process, considering the sorption equilibrium coefficient Ko, is given by the Eq. (3)

$$\Delta G^{\circ} = -RT \ln K_0 \tag{3}$$

where ΔG° is the standard free energy of sorption (kJ/mol), T is the temperature in Kelvin and R is the universal gas constant(8.314 J mol^{-1} K^{-1}). The sorption distribution coefficient Ko, was determined from the slope of the plot of ln(q_e/Ce) against Ce at different temperatures and extrapolated to zero Ce according to method suggested

Thermodynamic parameters		Parameters of adsorbent
ΔG°(kJ mol^{-1})	293K	− 0.79
	303K	− 0.75
	313K	− 0.69
ΔH°(kJ mol^{-1})	− 3.82	
ΔS°(J mol^{-1} K^{-1})	− 6.42	

Table 4. Thermodynamic parameters of the adsorbent.

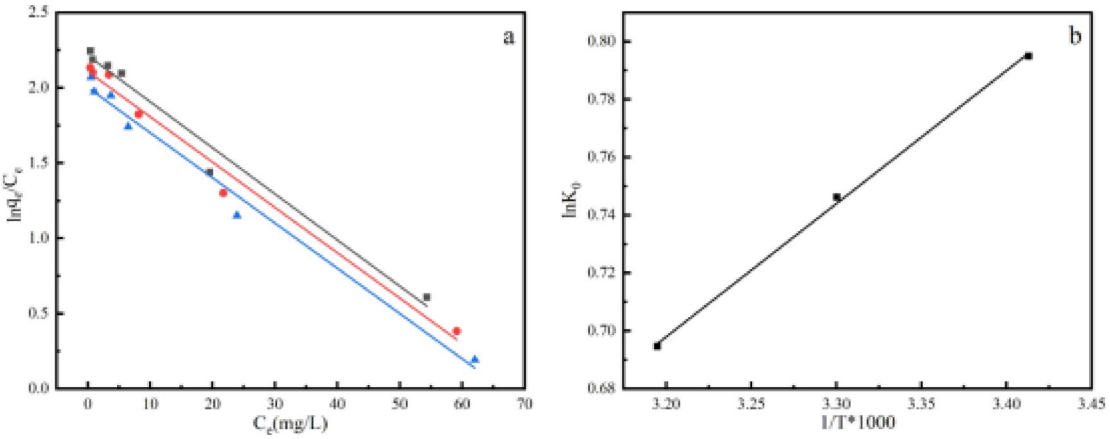

Fig. 11. (**a**) lnq$_e$/Ce against Ce (**b**) lnK$_0$ against 1/T*1000.

by Khan and Singh[44], The sorption distribution coefficient may be expressed in terms of ΔH° and ΔS° as a function of temperature:

$$\ln\ K_0 = \frac{\Delta S^\circ}{R} - \frac{\Delta H^\circ}{RT} \tag{4}$$

whereΔH° is the standard enthalpy change (kJ/mol) and ΔS° is the standard entropy change (kJ/mol K). The values of ΔH° and ΔS° can be obtained from the slope and intercept of a plot of lnK0 against 1/T*1000[35].The calculated values of thermodynamic parameters are shown in Table 4 and Fig. 11. The slope and intercept of the lnK$_0$ versus 1/T plot were used to determine ΔH° and ΔS°. The obtained values (Table 4) reveal that all ΔG° values are negative, confirming that fluoride adsorption on the Ce–H_2O_2 system is spontaneous. The negative ΔH° (− 3.82 kJ·mol^{-1}) indicates an exothermic process, whereas the negative ΔS° (− 6.42 J·mol^{-1}·K^{-1}) suggests that the adsorbent surface becomes more ordered after fluoride attachment.

Overall, the adsorption process is spontaneous and thermodynamically favorable, and is driven mainly by chemical interactions between Ce species and fluoride ions.

Regeneration and reusability study

The practical application of an adsorbent is highly dependent on its regeneration capability and reusability. To evaluate this, the adsorbent was subjected to three consecutive adsorption–desorption cycles. The fluoride removal performance across these cycles is compared with that of the initial cycle in Fig. 12.

The fresh adsorbent exhibited an initial adsorption capacity of 80.6 mg/g. After three regeneration cycles, the capacity was maintained at 50.6 mg/g, corresponding to a retention of approximately 63% of its original efficiency. The observed decline in capacity can be primarily attributed primarily to two factors: (1) the irreversible chemisorption of a fraction of fluoride ions onto strongly binding sites, rendering them unavailable for subsequent cycles; and (2) the inevitable physical loss of adsorbent mass during the filtration and washing steps of the regeneration process.

Despite the gradual decrease, the fact that the adsorbent retains significant adsorption capacity after multiple cycles demonstrates a satisfactory level of stability and reusability. This regenerative performance underscores the potential for repeated use of the adsorbent, which is a crucial factor for reducing operational costs and enhancing the economic feasibility of the adsorption process in practical wastewater treatment applications.

Defluoridation mechanism

The primary mechanisms underlying fluoride removal by Ce include electrostatic interactions, complexation, and ion exchange, as illustrated in the accompanying Fig. 13. Both Ce^{3+} and Ce^{4+} interact with fluoride ions through complexation and electrostatic interaction mechanisms[45]. Additionally, the presence of OH^- within the cerium structure facilitates fluoride removal via ion exchange, wherein OH^- ions are substituted by fluoride

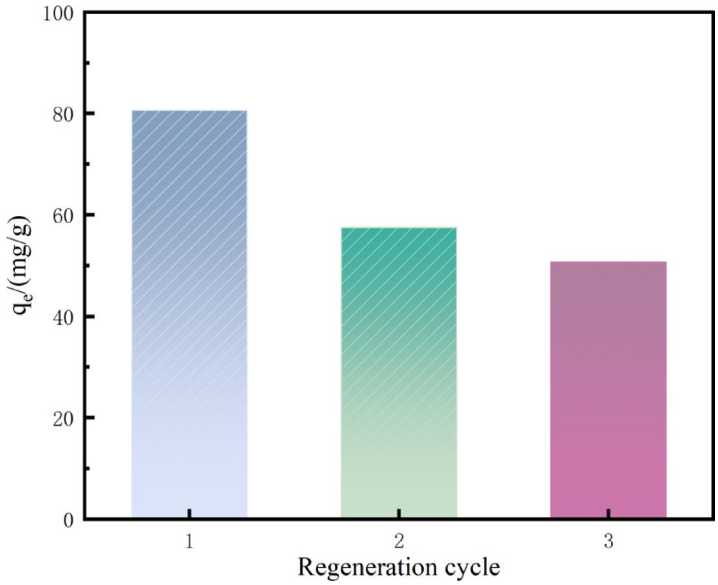

Fig. 12. Reusability of the adsorbent through three consecutive adsorption–desorption cycles (initial pH = 6.5, initial fluoride concentration = 100 mg L^{-1}, adsorbent dosage = 1 g L^{-1}, contact time = 120 min).

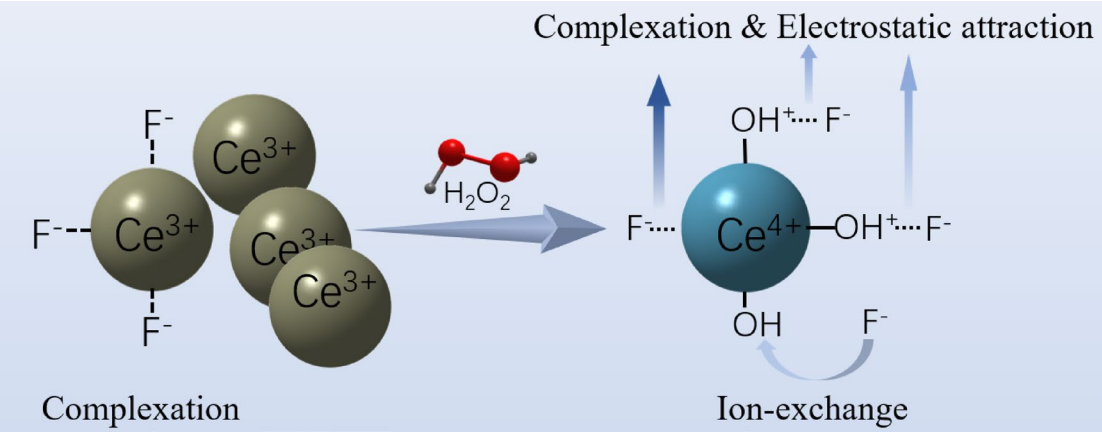

Fig. 13. Mechanism of fluoride adsorption.

ions[46]. These mechanisms were confirmed through FTIR and XPS analyses. On the basis of the adsorption behaviour, FTIR and XPS data, we propose that the process of fluoride removal by the adsorbent can be divided into two steps. First, a portion of Ce^{3+} reacts with F^- to form CeF_3, whereas the remaining Ce^{3+} is oxidised to Ce^{4+} by hydrogen peroxide. Ce^{4+} undergoes hydrolysis to generate Ce^{4+}–OH, and some fluorides are electrostatically adsorbed (outer complexation). Then, fluoride replaces OH– and binds itself to Ce.

Conclusions

This study demonstrated that the adsorbent system utilizing Ce^{3+} and H_2O_2 is a high-performance, cost-effective, and robust solution for water defluoridation, achieving a high adsorption capacity (up to 118.43 mg/g), maintaining efficiency over a wide pH range (5.0–8.0), and good resistance to coexisting anions.

The characterization results revealed two complementary defluoridation mechanisms: precipitation of thermodynamically stable CeF_3 and H_2O_2-induced oxidation,which results in the formation of Ce^{4+}–OH surface sites that capture residual fluoride through ligand exchange. XRD and XPS analyses confirmed the coexistence of the CeF_3 and CeO_2 phases, verifying this dual mechanism.

Thermodynamic studies indicated that the adsorption process was spontaneous and exothermic, and regeneration tests revealed ed that the material retained more than 60% of its capacity after three cycles, demonstrating good reusability. This simple, ambient-conditions synthesis using inexpensive precursors highlights the practical potential of the Ce^{3+}/H_2O_2 system for sustainable fluoride removal.

In addition to reporting a highly effective adsorbents, this work provides a deeper mechanistic understanding and introduces a new strategy for designing rare-earth-based materials for sustainable water purification. These

insights not only advance the scientific basis of fluoride adsorption but also guide the development of next-generation, high-performance, and low-cost defluoridation technologies. In future work, this system will be further optimized for continuous-flow operation and tested with real fluoride-containing industrial effluents to evaluate its field applicability. Additionally, efforts will focus on improving regeneration efficiency and extending the mechanism to other rare-earth-based adsorbents for multi-ion removal.

Data availability

All data generated or analyzed during this study are included in this article and its supplementary information files.

Received: 13 September 2025; Accepted: 30 October 2025
Published online: 28 November 2025

References

1. Abtahi, M. et al. Age-sex specific disability-adjusted life years (DALYs) attributable to elevated levels of fluoride in drinking water: A national and subnational study in Iran, 2017. *Water Res.* **157**, 94–105. https://doi.org/10.1016/j.watres.2019.03.087 (2019).
2. Cotruvo, J. A. (2017) 2017 Who Guidelines for Drinking Water Quality: First Addendum to the Fourth Edition. *J. Am. Water Works Ass.* **109**, 44–51, https://doi.org/10.5942/jawwa.2017.109.0087.
3. Hossain, M. & Patra, P. K. Hydrogeochemical characterisation and health hazards of fluoride enriched groundwater in diverse aquifer types. *Environ. Pollut.* **258**, 113646. https://doi.org/10.1016/j.envpol.2019.113646 (2020).
4. National Environmental Protection Agency of, C. Integrated Wastewater Discharge Standard (GB 8978-1996). (China Environmental Science Press, 1996).
5. Santhi, V. M. et al. The global challenge of fluoride contamination: A comprehensive review of removal processes and implications for human health and ecosystems. *Sustainability* **16**, 11056. https://doi.org/10.3390/su162411056 (2024).
6. Lobo, C. C., Lerner, J. E. C., Bertola, N. C. & Zaritzky, N. E. Synthesis and characterization of functional calcium-phosphate-chitosan adsorbents for fluoride removal from water. *Int. J. Biol. Macromol.* **264**, 130553. https://doi.org/10.1016/j.ijbiomac.2024.130553 (2024).
7. Yang, Y., Zhang, Z., Wang, Z., Liu, H. Y. & Sun, Z. X. Formation of high fluoride groundwater and associated health risks in the Cangzhou area of the North China Plain. *Environ. Earth Sci.* **84**, 111. https://doi.org/10.1007/s12665-025-12127-1 (2025).
8. Millar, G. J., CouperthWaite, S. J., Dawes, L. A., Thompson, S. & Spencer, J. Activated alumina for the removal of fluoride ions from high alkalinity groundwater: New insights from equilibrium and column studies with multicomponent solutions. *Sep. Purif. Technol.* **187**, 14–24. https://doi.org/10.1016/j.seppur.2017.06.042 (2017).
9. Zhou, N. et al. Enhanced fluoride removal from drinking water in wide pH range using La/Fe/Al oxides loaded rice straw biochar. *Water Supply* **22**, 779–794. https://doi.org/10.2166/ws.2021.232 (2022).
10. Zhou, Q. S. et al. Efficient removal of fluoride from water: Adsorption performance of MgO-x adsorbents derived from Mg-MOF-74 and insights from DFT calculations. *Sep. Purif. Technol.* **352**, 128190. https://doi.org/10.1016/j.seppur.2024.128190 (2025).
11. Dou, X. M., Zhang, Y. S., Wang, H. J., Wang, T. J. & Wang, Y. L. Performance of granular zirconium-iron oxide in the removal of fluoride from drinking water. *Water Res.* **45**, 3571–3578. https://doi.org/10.1016/j.watres.2011.04.002 (2011).
12. Wu, J. C., Chen, S. S., Yu, T. C., Wu, K. C. W. & Hou, C. H. Effective electrochemically controlled removal of fluoride ions using electrodeposited polyaniline-carbon nanotube composite electrodes. *Sep. Purif. Technol.* **254**, 117561. https://doi.org/10.1016/j.seppur.2020.117561 (2021).
13. Maliyekkal, S. M., Sharma, A. K. & Philip, L. Manganese-oxide-coated alumina: A promising sorbent for defluoridation of water. *Water Res.* **40**, 3497–3506. https://doi.org/10.1016/j.watres.2006.08.007 (2006).
14. Mir, N. et al. Self-separation of the adsorbent after recovery of rare-earth metals: Designing a novel non-wettable polymer. *Sep. Purif. Technol.* **259**, 118152. https://doi.org/10.1016/j.seppur.2020.118152 (2021).
15. Tokunaga, S. et al. Removal of fluoride ions from aqueous solutions by multivalent metal compounds. *Int. J. Environ. Stud.* **48**, 17–28 (1995).
16. Raichur, A. M. & Basu, M. J. Adsorption of fluoride onto mixed rare earth oxides. *Sep. Purif. Technol.* **24**, 121–127. https://doi.org/10.1016/S1383-5866(00)00219-7 (2001).
17. Gonzales, J. M. *Fluoride and Phosphate Removal From Industrial and Domestic Wastewaters Using Cerium Chloride* (University of Nevada, 2015).
18. Zúñiga-Muro, N. M., Bonilla-Petriciolet, A., Mendoza-Castillo, D. I., Reynel-Avila, H. E. & Tapia-Picazo, J. C. Fluoride adsorption properties of cerium-containing bone char. *J. Fluor. Chem.* **197**, 63–73. https://doi.org/10.1016/j.jfluchem.2017.03.004 (2017).
19. Wu, L. Y., Zhang, G. K. & Tang, D. D. A novel high efficient Mg-Ce-La adsorbent for fluoride removal: Kinetics, thermodynamics and reusability. *Desalin. Water Treat.* **57**, 23844–23855. https://doi.org/10.1080/19443994.2016.1138331 (2016).
20. He, Y. X. et al. Enhanced fluoride removal from water by rare earth (La and Ce) modified alumina: Adsorption isotherms, kinetics, thermodynamics and mechanism. *Sci. Total Environ.* **688**, 184–198. https://doi.org/10.1016/j.scitotenv.2019.06.175 (2019).
21. El Messaoudi, N. et al. Advances and future perspectives of water defluoridation by adsorption technology: A review. *Environ. Res.* **252**, 118857. https://doi.org/10.1016/j.envres.2024.118857 (2024).
22. El Messaoudi, N. *et al. Chapter Fourteen - Green synthesis of nanoparticles for remediation organic pollutants in wastewater by adsorption. In Advances in Chemical Pollution, Environmental Management and Protection.* **10**, 305–345 (Elsevier, 2023).
23. El Messaoudi, N. et al. Comprehensive analytical review of heavy metal removal efficiency using agricultural solid waste-based bionanocomposites. *Nano-Struct. Nano-Objects* **38**, 101220. https://doi.org/10.1016/j.nanoso.2024.101220 (2024).
24. Liang, P., Zhang, Y., Wang, D. F., Xu, Y. & Luo, L. Preparation of mixed rare earths modified chitosan for fluoride adsorption. *J. Rare Earth* **31**, 817–822. https://doi.org/10.1016/S1002-0721(12)60364-0 (2013).
25. Jeyaseelan, A., Kumar, I. A., Naushad, M. & Viswanathan, N. Fabrication of hydroxyapatite embedded cerium-organic frameworks for fluoride capture from water. *J. Mol. Liq.* **354**, 118830. https://doi.org/10.1016/j.molliq.2022.118830 (2022).
26. Raghav, S., Jain, P. & Kumar, D. Assembly of cerium impregnated pectin/silica–gel biopolymeric material for effective utilization for fluoride adsorption studies. *Mater. Today Proc.* **50**, 273–281. https://doi.org/10.1016/j.matpr.2021.06.327 (2022).
27. Tamboli, A. H., Jadhav, A. R., Chung, W. J. & Kim, H. Structurally modified cerium doped hydrotalcite-like precursor as efficient catalysts for hydrogen production from sodium borohydride hydrolysis. *Energy* **93**, 955–962. https://doi.org/10.1016/j.energy.2015.09.059 (2015).
28. Wu, P. et al. Simultaneous sorption of arsenate and fluoride on calcined Mg–Fe–La hydrotalcite-like compound from water. *ACS Sustain. Chem. Eng.* **6**, 16287–16297. https://doi.org/10.1021/acssuschemeng.8b03209 (2018).
29. Wan, D., Liu, Y., Chen, J., Zhang, J. & Xiao, S. Uptake fluoride from water by calcined Mg-Al-CO3 hydrotalcite: Mg/Al ratio effect on its structure, electrical affinity and adsorptive property. *Colloids Surf. A Physicochem. Eng. Asp.* **469**, 307–314 (2015).

30. Jeyaseelan, A., Viswanathan, N., Kumar, I. A. & Naushad, M. Design of hydrotalcite and biopolymers entrapped tunable cerium organic cubic hybrid material for superior fluoride adsorption. *Colloid Surface B.* **224**, 113190. https://doi.org/10.1016/j.colsurfb.2023.113190 (2023).
31. Seal, S. et al. Engineered defects in cerium oxides: Tuning chemical reactivity for biomedical, environmental, & energy applications. *Nanoscale* **12**, 6879–6899. https://doi.org/10.1039/d0nr01203c (2020).
32. Ahmad, S., Gopalaiah, K., Chandrudu, S. N. & Nagarajan, R. Anion (Fluoride)-doped ceria nanocrystals: Synthesis, characterization, and its catalytic application to oxidative coupling of benzylamines. *Inorg. Chem.* **53**, 2030–2039. https://doi.org/10.1021/ic403166q (2014).
33. Kumar, A., Babu, S., Karakoti, A. S., Schulte, A. & Seal, S. Luminescence properties of Europium-doped cerium oxide nanoparticles: Role of vacancy and oxidation states. *Langmuir* **25**, 10998–11007. https://doi.org/10.1021/la901298q (2009).
34. Slater, J. C. Atomic radii in crystals. *J. Chem. Phys.* **41**, 3199–3204. https://doi.org/10.1063/1.1725697 (1964).
35. Senol, Z. M., Arslanoglu, H., Keskin, Z. S., Mehmeti, V. & El Messaoudi, N. Biosorption of rhodamine B and sunset yellow dyes on cross-linked chitosan-alginate biocomposite beads: Experimental and theoretical studies. *Int. J. Biol. Macromol.* **298**, 139264. https://doi.org/10.1016/j.ijbiomac.2024.139264 (2025).
36. Liu, L., Cui, Z. J., Ma, Q. C., Cui, W. & Zhang, X. One-step synthesis of magnetic iron-aluminum oxide/graphene oxide nanoparticles as a selective adsorbent for fluoride removal from aqueous solution. *RSC Adv.* **6**, 10783–10791. https://doi.org/10.1039/c5ra23676b (2016).
37. Zhou, J. Y., Liu, Y. Y., Han, Y. T., Jing, F. Q. & Chen, J. W. Bone-derived biochar and magnetic biochar for effective removal of fluoride in groundwater: Effects of synthesis method and coexisting chromium. *Water Environ. Res.* **91**, 588–597. https://doi.org/10.1002/wer.1068 (2019).
38. Wang, J., Wu, L. Y., Li, J., Tang, D. D. & Zhang, G. K. Simultaneous and efficient removal of fluoride and phosphate by Fe-La composite: Adsorption kinetics and mechanism. *J. Alloy Compd.* **753**, 422–432. https://doi.org/10.1016/j.jallcom.2018.04.177 (2018).
39. Dong, S. X. & Wang, Y. L. Characterization and adsorption properties of a lanthanum-loaded magnetic cationic hydrogel composite for fluoride removal. *Water Res.* **88**, 852–860. https://doi.org/10.1016/j.watres.2015.11.013 (2016).
40. Zhou, J. et al. Highly selective and efficient removal of fluoride from ground water by layered Al-Zr-La Tri-metal hydroxide. *Appl. Surf. Sci.* **435**, 920–927. https://doi.org/10.1016/j.apsusc.2017.11.108 (2018).
41. Mei, L. P. et al. One-step synthesis of zirconium dioxide-biochar derived from seed shell with enhanced removal capacity for fluoride from water. *Appl. Surf. Sci.* **509**, 144685. https://doi.org/10.1016/j.apsusc.2019.144685 (2020).
42. Wang, A. H. et al. Granular tri-metal oxide adsorbent for fluoride uptake: Adsorption kinetic and equilibrium studies. *J. Colloid Interf. Sci.* **505**, 947–955. https://doi.org/10.1016/j.jcis.2017.06.074 (2017).
43. Wang, J. G., Chen, N., Li, M. & Feng, C. P. Efficient removal of fluoride using polypyrrole-modified biochar derived from slow pyrolysis of pomelo peel: Sorption capacity and mechanism. *J. Polym. Environ.* **26**, 1559–1572. https://doi.org/10.1007/s10924-017-1061-y (2018).
44. Asif, A., Khan, A. & Singh, R. P. Adsorption thermodynamics of carbofuran on Sn(IV) arsenosilicate in H^+, Na^+ and Ca^{2+} forms. *Colloids Surf.* **24**, 33–42 (1987).
45. Rego, R. M. et al. Cerium based UiO-66 MOF as a multipollutant adsorbent for universal water purification. *J. Hazard Mater.* **416**, 125941. https://doi.org/10.1016/j.jhazmat.2021.125941 (2021).
46. Tang, X. F. et al. Recent advances in metal-organic framework-based materials for removal of fluoride in water: Performance, mechanism, and potential practical application. *Chem. Eng. J.* **446**, 137299. https://doi.org/10.1016/j.cej.2022.137299 (2022).

Acknowledgements

This work was supported by the Major Science and Technology Special Project of Xinjiang Uygur Autonomous Region (2024A03008-2).

Author contributions

H.W.D. conceived and designed the study, performed the experiments, analyzed the data, and drafted the manuscript. L.X.F. and X.H.S. contributed to materials preparation and experimental assistance. T.T.L. and Z.F.S. assisted with data analysis and figure preparation. J.S.Z. contributed to literature review and discussion. K.L. supervised the project, provided critical revisions, and acted as the corresponding author. All authors reviewed and approved the final manuscript.

Funding

This research was funded by the Major Science and Technology Special Project of Xinjiang Uygur Autonomous Region (2024A03008-2).

Declarations

Competing interests

The authors declare no competing interests.

Additional information

Supplementary Information The online version contains supplementary material available at https://doi.org/10.1038/s41598-025-26780-w.

Correspondence and requests for materials should be addressed to K.L.

Reprints and permissions information is available at www.nature.com/reprints.

Publisher's note Springer Nature remains neutral with regard to jurisdictional claims in published maps and institutional affiliations.